Spatiotemporal Assessment of Inland Reservoir Water Quality Using Sentinel-2 Imagery and a Quasi-Analytical Algorithm

Balaji B. Yadav[1], Digambar A. Solanke[2], Vikas V. Ghodke[3], Rohit A. Kargude[4], Sandipan S. Sawant[5], Shafiyoddin Sayyad[6]

[1,2,3,4,5] *Department of physics, Shri Chhatrapati Shivaji College, Omerga, Dharashiv, Maharashtra, India*

[6] *Microwave & Imaging Spectroscopy Laboratory, Miliiya College, Beed, Maharashtra, India*

doi.org/10.64643/IJIRTV12I8-191977-459

***Abstract*—Degradation of water quality in inland reservoirs presents a major challenge for sustainable water resource management, particularly in data-scarce regions of developing countries. This study provides a spatiotemporal assessment of water quality in Majalgaon Dam, Maharashtra, India, using multispectral Sentinel-2 imagery integrated with a Quasi-Analytical Algorithm (QAA). Satellite observations were employed to derive spatially distributed estimates of total suspended solids (TSS) and chlorophyll-a (Chl-a) based on bio-optical modeling, while the Normalized Difference Water Index (NDWI) was used to accurately delineate the reservoir extent. To demonstrate calibration and validation workflows in the absence of concurrent field campaigns, a synthetic dataset comprising 50 stratified sampling locations was generated under realistic measurement assumptions. The analysis revealed strong spatial heterogeneity, with elevated TSS near tributary inflows, moderate concentrations in shallow near-shore zones, and consistently lower levels in the central basin. Chlorophyll-a exhibited a partially decoupled spatial pattern, with localized biomass enhancement in sheltered embayments. Seasonal analysis for 2023 indicated pronounced monsoon-driven dynamics, characterized by increased TSS during monsoon months and higher Chl-a during post-monsoon periods. Multi-year analysis (2018–2023) showed substantial inter-annual variability linked to climatic and watershed controls. While linear calibration using synthetic data showed limitations in absolute concentration accuracy, satellite-derived products effectively preserved relative spatial and temporal patterns. The results highlight the utility of Sentinel-2–based remote sensing as a scalable and cost-effective approach for reservoir water quality monitoring and management.**

***Index Terms*—Water quality monitoring, Sentinel-2 multispectral imagery, Quasi-Analytical Algorithm, Total suspended solids, Chlorophyll-a, Remote sensing, Bio-optical modelling, Spatiotemporal variability, Inland reservoirs, Reservoir management.**

I. INTRODUCTION

1.1 Global Water Quality Challenges

Freshwater reservoirs represent indispensable components of global water infrastructure, supporting agricultural irrigation, municipal drinking water supply, hydropower generation, fisheries, and recreational activities. These inland water bodies underpin food security, economic stability, and ecosystem services for millions of people worldwide[1]. However, rapid population growth, agricultural intensification, industrial expansion, and unplanned urbanization have exerted unprecedented pressure on freshwater systems. Nutrient enrichment from agricultural runoff, discharge of inadequately treated industrial effluents, and alterations in watershed hydrology due to land-use change have collectively accelerated the degradation of water quality in reservoirs and lakes[2].

Globally, deteriorating water quality manifests through eutrophication, increased turbidity, harmful algal blooms, sediment accumulation, and biodiversity loss. These impacts extend beyond ecological consequences to include serious public health risks, economic losses, and social inequities. Nutrient-enriched waters often promote cyanobacterial blooms that produce toxins resistant to conventional treatment processes, posing direct threats to drinking water safety. Excessive sedimentation reduces reservoir storage capacity, shortens infrastructure lifespan, and

compromises water supply reliability. Furthermore, declining water quality adversely affects fisheries, tourism, and cultural ecosystem services, disproportionately impacting communities dependent on inland water resources for livelihoods[3].

1.2 Constraints of Conventional Monitoring Approaches

Water quality assessment has traditionally relied on in situ sampling and laboratory-based analysis of physical, chemical, and biological parameters. While such methods provide precise point-based measurements, they are constrained by high operational costs, logistical complexity, and limited spatiotemporal coverage. Field sampling requires trained personnel, site accessibility, and careful sample handling, while laboratory analysis entails additional time delays and specialized instrumentation[4]. These challenges are particularly pronounced in developing countries, where financial and technical resources for sustained monitoring programs are often limited. As a result, conventional monitoring is typically restricted to a small number of fixed stations and infrequent sampling intervals, often monthly or quarterly. This sparse coverage fails to capture the inherent spatial heterogeneity of large reservoirs, where water quality varies due to tributary inflows, circulation dynamics, bathymetry, and localized biological activity. Similarly, episodic events such as sediment plumes, pollution discharges, or rapid algal bloom development may remain undetected between sampling campaigns. Consequently, traditional monitoring approaches provide an incomplete representation of system dynamics, limiting their effectiveness for early warning, trend detection, and adaptive water resource management[5].

1.3 Satellite Remote Sensing for Inland Water Assessment

Satellite remote sensing has emerged as a powerful alternative and complement to field-based monitoring, offering synoptic, repetitive, and cost-effective observations of inland water bodies. Optical satellite sensors measure water-leaving radiance, which encodes information about optically active constituents such as suspended sediments, phytoplankton pigments, and colored dissolved organic matter[6]. The interaction of sunlight with these constituents produces distinctive spectral responses that can be quantified using multispectral and hyperspectral imagery. The principal advantage of satellite observations lies in their ability to provide spatially continuous coverage of entire reservoirs at frequent revisit intervals, enabling the monitoring of spatial gradients and temporal dynamics that are impractical to observe using in situ methods alone. Contemporary Earth observation missions offer revisit frequencies ranging from days to weeks, facilitating the tracking of seasonal variability, monsoon-driven processes, and short-term disturbance events[7]. Moreover, the digital and geospatial nature of satellite data enables efficient processing, long-term archival, and integration with ancillary datasets for advanced analysis and visualization. Among available platforms, the Sentinel-2 constellation of the European Space Agency represents a major advancement for inland water quality monitoring. The constellation provides multispectral imagery in 13 bands spanning visible to shortwave infrared wavelengths, with spatial resolutions of 10–20 m for water-relevant bands and a revisit frequency of approximately five days. Importantly, Sentinel-2 data are freely accessible under the Copernicus program, substantially lowering barriers to operational monitoring in data-scarce regions[8].

1.4 Bio-Optical Modeling and the Quasi-Analytical Algorithm

Retrieving quantitative water quality parameters from satellite data requires robust bio-optical algorithms that relate measured reflectance to constituent concentrations. Empirical approaches, which establish statistical relationships between spectral indices and in situ measurements, are computationally efficient but often lack physical interpretability and exhibit limited transferability beyond calibration conditions. In contrast, fully analytical radiative transfer models are physically rigorous but require extensive ancillary data and significant computational resources[9]. The Quasi-Analytical Algorithm (QAA) provides a balanced alternative by integrating radiative transfer theory with practical computational efficiency. QAA estimates inherent optical properties, including absorption and backscattering coefficients, directly from remote sensing reflectance without extensive site-specific calibration. Through a stepwise inversion procedure, the algorithm derives particulate

backscattering at a reference wavelength, estimates its spectral dependence, and subsequently retrieves absorption coefficients across wavelengths. These inherent optical properties can then be linked to water quality parameters such as total suspended solids and chlorophyll-a concentrations[10]. The semi-analytical foundation of QAA enhances its physical interpretability and transferability across diverse optical water types, including complex inland reservoirs. Its modest input requirements and computational simplicity make it well suited for operational applications using satellite platforms such as Sentinel-2.

1.5 Objectives and Significance of the Study

The present study aims to demonstrate the operational feasibility of satellite-based water quality assessment for inland reservoirs using Sentinel-2 imagery and bio-optical modeling. The specific objectives are to (i) delineate reservoir water bodies using spectral water indices, (ii) implement the Quasi-Analytical Algorithm to retrieve key water quality parameters, (iii) calibrate and validate satellite-derived estimates using simulated ground-reference data and statistical performance metrics, and (iv) analyze spatiotemporal patterns of water quality over an annual cycle. Beyond the selected case study, the proposed framework is designed to be transferable to other reservoirs with minimal modification. By leveraging freely available satellite data and cloud-based processing platforms, the approach reduces financial and computational constraints that often limit large-scale monitoring efforts. The integration of satellite observations with targeted field data supports a hybrid monitoring strategy that enhances spatial coverage, temporal resolution, and decision-making capacity. Overall, this study contributes to the growing evidence that satellite remote sensing has matured into a reliable and scalable tool for inland water quality management.

II. MATERIALS AND METHODS

2.1 Study Area Description and Characterization

The study area encompasses the Majalgaon subdistrict within Beed District of Maharashtra State, India. For administrative and technical purposes within the geospatial analysis workflow, the district is denoted as "B|D" in the boundary dataset. The study area was defined using an administrative boundary feature collection that provides subdistrict-level polygons for the entire region. Filtering operations were applied to extract specifically the Majalgaon subdistrict boundary, which served as the spatial extent for all subsequent image processing and analysis operations Figure 1.The study area boundary was used to center the interactive mapping interface and to clip satellite imagery products to the region of interest, ensuring computational efficiency by limiting processing to the relevant geographic extent.

Figure 1. Study area map showing Majalgaon subdistrict boundary in Beed District, Maharashtra, India and With Sentinel-2 true color imagery and major water bodies identified within the region.

Figure 2 NDWI-based delineation of surface water bodies in the Majalgaon study area. All significant water bodies with an aerial extent greater than 1 ha are extracted using threshold-based classification of the Normalized Difference Water Index (NDWI) and displayed in cyan . The Majalgaon Dam, identified as the largest and most dominant surface water feature within the study area, is highlighted in red color, with a mapped surface area of 40,882,258.58 m². As illustrated in Fig. 2, the Majalgaon Dam represents the principal hydrological feature of the region in terms of spatial extent and influence. The reservoir exhibits an elongated, valley-controlled morphology characteristic of riverine impoundments, where inundation follows the pre-existing river channel and extends into multiple tributary arms. This geomorphic configuration results in pronounced bathymetric variability, with comparatively deeper zones along the former river course and extensive shallow regions within flooded side valleys and embayments. The shoreline geometry comprises a combination of natural terrain-controlled margins and engineered

sections associated with dam infrastructure. Such morphological complexity, clearly captured by the NDWI-derived water boundary in Fig. 2, contributes to spatial heterogeneity in hydrodynamic processes and water quality parameters. Accurate delineation of the reservoir and associated water bodies was therefore essential for reliable interpretation of satellite-derived water quality indicators and for the design of spatially representative sampling and zonal analysis frameworks.

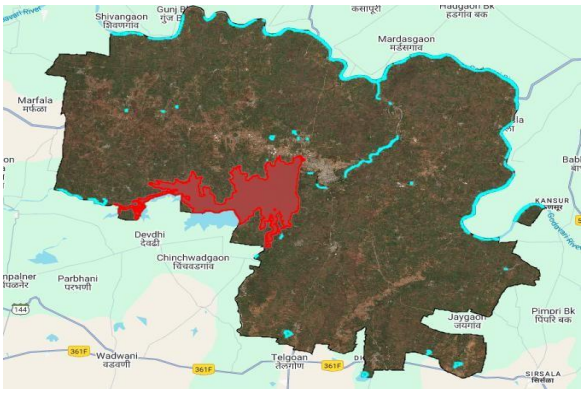

Figure 2. NDWI-based water body delineation of the Majalgaon study area.

III. SATELLITE DATA ACQUISITION AND PRE-PROCESSING

3.1 Sentinel-2 Data and Sensor Characteristics

Multispectral satellite data from the European Space Agency's Sentinel-2 mission were used as the primary data source for this study. The Sentinel-2 constellation consists of two identical satellites (Sentinel-2A and Sentinel-2B) carrying the Multispectral Instrument (MSI), which acquires imagery in 13 spectral bands spanning the visible, near-infrared, and shortwave infrared regions at spatial resolutions of 10, 20, and 60 m. The satellites operate in a sun-synchronous orbit at an altitude of approximately 786 km, providing a combined revisit time of about five days. This high temporal frequency, together with stable radiometric calibration and 12-bit quantization, makes Sentinel-2 particularly suitable for quantitative inland water studies. Level-2A surface reflectance products from the harmonized Sentinel-2 archive (COPERNICUS/S2_SR_HARMONIZED) were accessed through Google Earth Engine. These products are atmospherically corrected using the Sen2Cor processor, which accounts for molecular scattering, aerosols, and gaseous absorption, ensuring radiometrically consistent bottom-of-atmosphere reflectance for multi-temporal analysis.

3.2 Spectral Band Selection and Water Quality Sensitivity

Six MSI bands were selected based on their relevance to optically active water constituents (**Figure 2**). The blue (490 nm) and green (560 nm) bands are sensitive to suspended sediments, colored dissolved organic matter, and chlorophyll-related reflectance. The red band (665 nm) coincides with strong chlorophyll-a absorption, while the red-edge bands at 705 and 740 nm enhance sensitivity to higher chlorophyll concentrations that often saturate red-band algorithms. The near-infrared band (842 nm), characterized by strong water absorption, was primarily used for water–land discrimination and suspended matter detection. Together, these bands cover the key spectral regions required for bio-optical modeling of total suspended solids and phytoplankton biomass, while the 10–20 m spatial resolution enables detailed mapping of intra-reservoir variability.

3.3 Image Quality Control and Compositing

Robust filtering and quality control were applied to ensure reliable analysis. Images acquired during 2023 were used for primary assessment, with additional data from 2018–2023 used for inter-annual analysis. Cloud contamination was minimized using the CLOUDY_PIXEL_PERCENTAGE metadata, applying a threshold of <10% for spatial composites and <20% for time-series analysis. Visual inspection was performed to remove scenes affected by residual cloud artifacts or atmospheric correction errors. To obtain a spatially consistent representation of reservoir conditions, a median composite image was generated from all quality-controlled scenes. Median compositing effectively suppresses outliers, residual cloud effects, and short-term hydrological noise, while improving spatial completeness (**Figure 3**). Compositing was restricted to pixels classified as water using NDWI-based masking, ensuring that the final composite provides a synoptic and spectrally consistent depiction of surface water conditions in Majalgaon Dam.

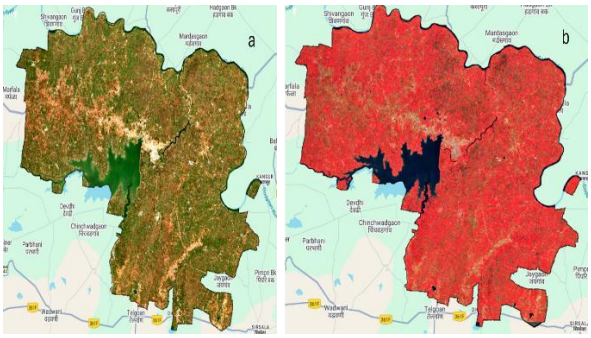

Figure 3: Sentinel-2 median composite imagery (2023) of Majalgaon Dam. (a) True color composite (RGB: B4–B3–B2) depicting the natural appearance of the reservoir and surrounding landscape. (b) False color composite (RGB: B8–B4–B3) highlighting vegetation in red and surface water in dark blue.

Accurate delineation of surface water is a fundamental prerequisite for satellite-based water quality analysis, as it defines the spatial domain over which bio-optical retrievals are valid. In this study, surface water bodies were extracted using the Normalized Difference Water Index (NDWI), which exploits the contrasting spectral behavior of water and terrestrial surfaces in the visible and near-infrared regions of the electromagnetic spectrum. Water exhibits relatively high reflectance in the green band and strong absorption in the near-infrared, whereas vegetation and built-up surfaces display low green reflectance and high near-infrared reflectance. This pronounced contrast enables robust discrimination of water pixels in multispectral imagery. For Sentinel-2 data, NDWI was computed using surface reflectance from the green band (Band 3; 560 nm) and the near-infrared band (Band 8; 842 nm) according to Eq. (1) and (2):

$$NDWI = \frac{(\rho\_green - \rho\_NIR)}{(\rho\_green + \rho\_NIR)} \ldots\ldots\ldots (1)$$

$$NDWI = \frac{(B3 - B8)}{(B3 + B8)} \ldots\ldots\ldots (2)$$

where ρ denotes surface reflectance. The normalized formulation constrains NDWI values to the range −1 to +1 and reduces sensitivity to illumination variability and residual atmospheric effects. NDWI was calculated using the median composite Sentinel-2 image to ensure spatial continuity and temporal representativeness of surface conditions across the study area. As illustrated in **Figure 4**, water bodies produce distinctly positive NDWI values, typically between 0.2 and 0.8, while vegetation yields strongly negative values and bare soil or built-up areas cluster near zero. The resulting NDWI map exhibits a clear bimodal value distribution, enabling reliable separation of water and non-water surfaces.

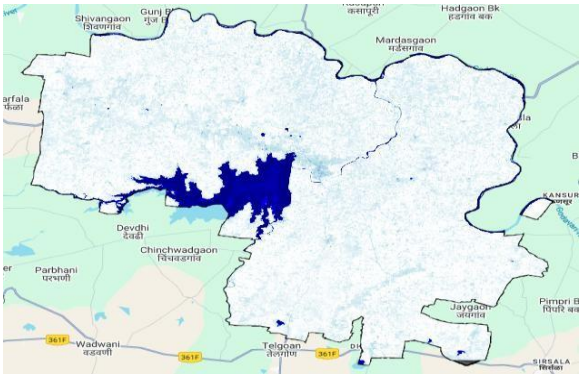

Figure 4. Normalized Difference Water Index (NDWI) visualized with blue color palette. The clear spectral separation enables robust water body delineation.

To convert continuous NDWI values into a binary classification, a threshold of NDWI > 0.1 was applied to identify water pixels. This relatively conservative threshold was selected based on prior inland water studies and careful visual inspection of NDWI histograms and spatial patterns, ensuring inclusion of turbid water areas that may exhibit reduced NDWI values due to enhanced near-infrared reflectance from suspended sediments. The selected threshold minimized omission errors while maintaining low commission errors when compared against true-color Sentinel-2 imagery. Pixels exceeding the threshold were classified as water, while all remaining pixels were masked as non-water, effectively isolating surface water for subsequent analysis. The resulting binary water mask was converted from raster to vector format to delineate individual water body polygons and compute their geometric properties. Polygon boundaries were generated by tracing water–land interfaces, and surface area was calculated in a projected coordinate system to ensure metric accuracy. To focus the analysis on significant and persistent water bodies, a minimum area threshold of 10,000 m² (1 ha) was applied, removing small ponds, ephemeral pools, and potential false detections. Among the remaining features, Majalgaon Dam was objectively identified as the largest water body based on surface area. The extracted dam polygon was subsequently

used to clip all satellite-derived products and define the spatial domain for water quality analysis. This automated and reproducible delineation approach eliminates the need for manual digitization and ensures consistent identification of the reservoir based solely on spectral characteristics.

IV. IMPLEMENTATION OF QUASI-ANALYTICAL ALGORITHM

4.1 Remote Sensing Reflectance Derivation

Quantitative bio-optical algorithms require input data in units of remote sensing reflectance (Rrs), which represents the water-leaving radiance normalized by downwelling irradiance. Remote sensing reflectance has units of inverse steradians (sr^{-1}) and typically ranges from 0 to 0.02 sr^{-1} for natural waters in the visible spectrum. Sentinel-2 Level-2A products provide surface reflectance, which approximates the fraction of incident irradiance that is reflected by the surface in a bidirectional sense. Conversion from surface reflectance to remote sensing reflectance requires accounting for the bidirectional nature of the measurement and normalizing by the solid angle subtended by the upwelling radiance field. The conversion was implemented through the following operations applied to each relevant spectral band:

$$Rrs(\lambda) = \frac{SR(\lambda)}{(10000 \times \pi)} \quad \text{.....(3)}$$

where SR(λ) is the surface reflectance value provided in the Sentinel-2 product (scaled by 10,000), π accounts for the angular distribution of upwelling light, and the result Rrs(λ) has units of sr^{-1}. This conversion was applied to Bands 2, 3, 4, 5, and 6, producing corresponding Rrs images at wavelengths 490, 560, 665, 705, and 740 nm. These converted bands formed the input dataset for subsequent bio-optical inversion through the Quasi-Analytical Algorithm. Spatial masking was applied to limit Rrs calculations to pixels identified as water in the NDWI-derived mask and specifically to pixels within the Majalgaon Dam boundary. This masking prevented calculation of meaningless Rrs values over terrestrial surfaces and focused computational resources on the water body of interest. The masked Rrs images maintained spatial correspondence with the original surface reflectance images, preserving the 10-20 meter resolution for water quality parameter derivation.

4.2 Fundamental Optical Properties and Constants

The QAA inversion procedure requires specification of pure water optical properties as known constants. These properties include the absorption coefficient (a_w) and backscattering coefficient (bb_w) of optically pure water as a function of wavelength. Values were adopted from the authoritative measurements of Pope and Fry (1997) for absorption and Smith and Baker (1981) for scattering. The absorption coefficient of pure water increases exponentially from blue to red wavelengths, with values of 0.015 m^{-1} at 490 nm, 0.0619 m^{-1} at 560 nm, and 0.429 m^{-1} at 665 nm. The backscattering coefficient of pure water follows approximately a $\lambda^{-4.32}$ spectral dependence, with values of 0.002 m^{-1} at 490 nm, 0.001 m^{-1} at 560 nm, and 0.0003 m^{-1} at 665 nm. These pure water properties represent the baseline optical characteristics that would be measured in perfectly clean water containing no dissolved or suspended constituents. Any deviation from these baseline properties in natural waters results from the presence of optically active materials including phytoplankton, suspended sediments, and colored dissolved organic matter. The QAA algorithm leverages this principle, using measured reflectance to estimate the total optical properties and then subtracting the known pure water contribution to isolate the properties attributable to natural water constituents. This decomposition enables linking optical measurements to constituent concentrations through established relationships.

4.3 Step-by-Step QAA Inversion Procedure

The QAA inversion followed the Lee et al. (2002) formulation adapted for application to inland waters. The algorithm progresses through a series of analytical steps, each building on results from previous steps to progressively refine estimates of inherent optical properties.

Step 1: Subsurface Remote Sensing Reflectance Ratio (u)

The first step calculates the subsurface remote sensing reflectance ratio, commonly denoted as Rrs. This ratio relates surface-measured remote sensing reflectance to the subsurface value, accounting for the refraction and reflection at the air-water interface. The empirical relationship developed by Gordon et al. (1988) and applied in QAA is:

$$u(\lambda) = \frac{Rrs(\lambda)}{[1.86 \times Rrs(\lambda) + 0.089]} \quad \text{.....} (4)$$

This transformation adjusts for the atmospheric-oceanic interface and relates the measured reflectance to the inherent optical properties. The u parameter is physically related to the ratio of backscattering to total absorption and backscattering. This step was computed separately for wavelengths 490, 560, and 665 nm, producing three u images corresponding to these key wavelengths.

Step 2: Particulate Backscattering at Reference Wavelength

Using the u value at 665 nm (red band) and the known pure water properties at this wavelength, the particulate backscattering coefficient bbp(665) was calculated through inversion of the quasi-single-scattering approximation:

$$bbp(665) = \frac{u(665) \times a_{w(665)}}{1 - u(665) \times bb_{w(665)}} \quad \text{.....} (5)$$

This equation isolates the backscattering contribution from particles by subtracting the known pure water backscattering from the total backscattering derived from the reflectance measurement. The 665 nm wavelength serves as the reference because at this red wavelength, phytoplankton absorption is typically negligible relative to water absorption in most natural waters, simplifying the inversion. The bbp(665) image represents a key intermediate product as particulate backscattering is directly related to suspended particle concentration.

Step 3: Spectral Slope Parameter (η)

The spectral dependence of particulate backscattering typically follows a power-law function $bbp(\lambda) \propto \lambda^{-\eta}$, where η is the spectral slope parameter. Values of η typically range from 0 to 2, with smaller particles producing steeper slopes (larger η). QAA estimates η from the spectral shape of reflectance using the empirical relationship:

$$\eta = \frac{2.0 \times 1 - 1.2exp(-0.9 \times Rrs(490))}{Rrs(560)} \quad \text{.....} (6)$$

This formulation relates the blue-to-green reflectance ratio to the particle spectral slope based on empirical analysis of diverse water types. The η parameter was calculated as an image, recognizing that particle size distributions may vary spatially across the reservoir due to sources, settling, and resuspension processes. *Step 4: Backscattering at Other Wavelengths*

With bbp(665) and η determined, the particulate backscattering coefficient at other wavelengths was calculated using the power-law relationship:

$$bbp(\lambda) = bbp(665) \times \left(\frac{665}{\lambda}\right)^{\eta} \quad \text{.....} (7)$$

This calculation was applied to derive bbp(560) and bbp(490), providing backscattering estimates across the visible spectrum. The spatially varying η parameter ensured that spectral extrapolation accounted for local particle characteristics.

Step 5: Absorption Coefficient Derivation

The final step inverted the reflectance relationship to solve for the absorption coefficient at 490 nm:

$$a(490) = \frac{[(1 - u(490)) \times (bbp(490) + bb_{w(490)})]}{u(490)} \quad \text{.....} (8)$$

This absorption coefficient represents the combined effects of pure water, phytoplankton pigments, colored dissolved organic matter, and non-algal particles. The 490 nm wavelength was selected because absorption at this blue wavelength is sensitive to dissolved organic matter, which often co-varies with terrestrial inputs and can provide insights into watershed processes. The complete QAA inversion produced spatially distributed images of particulate backscattering at multiple wavelengths and absorption at 490 nm, representing the inherent optical properties of Majalgaon Dam waters. These optical properties served as intermediate products for deriving water quality parameters of management relevance.

4.4 Water Quality Parameter Derivation from Optical Properties

4.4.1 Total Suspended Solids (TSS) Estimation

Total suspended solids concentration represents the dry mass of all particles (organic and inorganic) suspended in the water column per unit volume, typically expressed in milligrams per liter (mg/L). TSS is a fundamental water quality parameter affecting water clarity, light penetration, habitat quality, and sedimentation processes. The concentration of suspended particles is directly related to the particulate backscattering coefficient because particles are the dominant source of light scattering in natural waters. The relationship between bbp and TSS has been established theoretically and empirically by numerous researchers. Nechad et al. (2010) demonstrated that TSS can be estimated from particulate backscattering through a linear or power-law relationship, with the

specific coefficients depending on particle composition and size distribution. For this study, we applied a simplified linear relationship:

$$TSS_{QAA} = bbp(665) \times 100 \quad \text{.....(9)}$$

The multiplicative factor of 100 converts the backscattering coefficient (units of m^{-1}) to an approximate TSS value. This factor represents an initial uncalibrated relationship that requires refinement through comparison with field measurements. The uncalibrated TSS_QAA product provides relative spatial and temporal patterns even before calibration, as variations in bbp(665) directly reflect variations in particle loading. The TSS_QAA image was calculated across the entire dam area, producing a spatially continuous map of relative suspended solids concentration. Higher values indicate zones with elevated particle concentrations, potentially associated with tributary inputs, resuspension by wind mixing, or biological productivity.

4.4.2 Chlorophyll-a (Chl-a) Concentration Estimation

Chlorophyll-a serves as a proxy for phytoplankton biomass and represents a critical indicator of trophic status and algal bloom risk. Chlorophyll-a exhibits strong absorption features in the blue (~440 nm) and red (~665 nm) portions of the spectrum, with a reflectance maximum in the green (~560 nm). Traditional chlorophyll algorithms exploit these spectral features through band ratios or differences. For turbid inland waters where, suspended sediments can interfere with blue and red band algorithms, red-edge bands have proven particularly effective. The red-edge region (700-720 nm) experiences strong sensitivity to chlorophyll absorption while being less affected by sediment backscattering. We implemented a red edge to red ratio algorithm following the approach of Gitelson et al. (2008):

$$Chl_{QAA} = \left[\frac{Rrs(705)}{Rrs(665)}\right]^2 \times 20 \ldots\ldots\ldots (10)$$

This formulation uses the squared ratio of Sentinel-2 Band 5 (705 nm, red-edge) to Band 4 (665 nm, red), amplifying the spectral contrast associated with chlorophyll absorption. The multiplicative factor of 20 scales the dimensionless ratio to approximate chlorophyll-a concentrations in units of micrograms per liter (µg/L), though calibration is required for quantitative accuracy. The squared ratio approach has theoretical justification from bio-optical modeling showing that reflectance ratios relate to the ratio of backscattering to absorption, which in turn relates to chlorophyll concentration through power-law functions. The red-edge band's position on the steep chlorophyll absorption edge provides high sensitivity particularly for moderate to high chlorophyll concentrations where red band algorithms may saturate. The Chl_QAA image was calculated across the dam, producing a spatial map of relative phytoplankton biomass. Combined with TSS_QAA and absorption coefficient a(490), these three parameters were composited into a multi-band water quality product.

4.5 Calibration and Validation Framework

4.5.1 Synthetic Field Data Generation

A critical requirement for operational water quality remote sensing is calibration of satellite-derived parameters against field measurements of actual constituent concentrations. In this methodological demonstration study, we generated a synthetic field dataset to simulate the calibration and validation process that would be applied with real field samples. The synthetic dataset was created by selecting 50 locations distributed across the dam using the stratified sampling design described in Section 2.8. For each synthetic sampling location, simulated measured values of TSS and Chl-a were generated using relationships that introduce realistic correlation with the satellite-derived parameters while adding stochastic variability to represent measurement uncertainty and natural variability. The generation process assigned measured values based on the sampling zone classification (Low/Medium/High TSS) with random noise to simulate field measurement precision. Specifically, simulated TSS_measured values ranged from approximately 20-70 mg/L with higher values in zones classified as high

TSS based on satellite observations. Simulated

Chl_measured values ranged from approximately 5-20 µg/L following similar patterns. Additional simulated parameters including turbidity and Secchi depth were also generated to represent typical field sampling protocols. All synthetic field locations were attributed with coordinates and sampling metadata including date (simulated as mid-year 2023) to represent the type of information that would be collected during actual

field surveys. This synthetic approach enabled

demonstration of the complete calibration workflow while acknowledging the limitation that results represent methodological illustration rather than validation against actual measurements. The manuscript explicitly documents this synthetic data approach to maintain scientific transparency and clarity regarding study limitations.

4.5.2 Temporal Matching of Satellite and Field Data

Robust validation of satellite-derived water quality products requires temporal matching between satellite observations and field sample collection. Water quality parameters can vary substantially over short time periods (days to weeks) due to weather events, hydrological changes, and biological dynamics. Ideally, field samples should be collected within ±3 hours of satellite overpass to ensure that measured and observed conditions correspond. For this study, synthetic field samples were assigned a collection date of June 15, 2023 (mid-year). To match this field campaign date, we constructed a robust satellite composite using all cloud-free Sentinel-2 acquisitions within a ±15-day window (May 31 - June 30, 2023). This 30-day window composite approach addresses a critical challenge in tropical/subtropical regions where clouds frequently prevent satellite observation on any specific date. Using a median composite over the temporal window increases the probability of obtaining valid observations while maintaining reasonable temporal proximity to the field sampling date. The temporal window composite applied the same cloud filtering thresholds (CLOUDY_PIXEL_PERCENTAGE < 20%) used for time series analysis. The median compositing operation effectively filtered residual cloud pixels and provided stable parameter estimates. Remote sensing reflectance was calculated from the window composite, and the QAA inversion procedure was applied to derive TSS_satellite and Chl_satellite products corresponding to the field sampling period.

4.5.3 Value Extraction at Field Locations

Satellite-derived water quality values were extracted at each of the 50 synthetic field sampling locations through spatial overlay operations. The reduceRegions function computed mean values of TSS_satellite and Chl_satellite within a small buffer around each point location. The 30-meter scale parameter ensured extraction at the native satellite resolution. This extraction process produced a feature collection where each field sampling location was attributed with both its simulated measured values and the corresponding satellite-derived values. Critical data quality procedures were implemented during extraction to handle potential null values that could arise from cloud contamination, land adjacency effects, or algorithm failures. The median composite approach substantially reduced null value occurrence by filling temporal gaps. Features with null satellite values were filtered from the validation dataset to ensure that accuracy statistics reflected only locations with valid satellite retrievals. Type casting operations explicitly converted all numeric values to the Number data type to prevent type errors during subsequent statistical calculations and charting operations. The cleaned validation dataset containing matched pairs of measured and satellite-derived values served as the basis for developing calibration equations and computing accuracy metrics. The matched dataset was exported as a CSV table for detailed examination and potential analysis in external statistical software

4.5.4 Calibration Equation Development

Empirical calibration equations were developed through linear regression between satellite-derived parameters (independent variables) and field-measured values (dependent variables). For each water quality parameter, the calibration equation takes the form:

$$Parameter_{calibrated} = slope \times Parameter_{satellite} + intercept \ldots\ldots\ldots (11)$$

In an operational study with actual field data, regression coefficients would be determined through least-squares fitting of the validation dataset. Standard regression diagnostics including coefficient of determination (R^2), root mean square error (RMSE), and inspection of residual patterns would inform assessment of regression model adequacy. For this demonstration study using synthetic data, illustrative calibration coefficients were specified based on expected relationships:

TSS Calibration:

$$TSS_{calibrated} = 1.25 \times TSS_{satellite} - 5.3 \ldots\ldots\ldots (12)$$

Chlorophyll-a Calibration:

$$Chl_{calibrated} = 0.88 \times Chl_{satellite} + 2.1 \ldots\ldots (13)$$

These coefficients represent the type of calibration that might emerge from actual field validation. The slope near 1.0 suggests that the QAA-derived parameters capture the relative magnitude of variability, while the intercept terms correct for systematic biases. In actual applications, these coefficients would be updated periodically as additional field data become available, progressively improving calibration accuracy.

4.6 Stratified Sampling Design for Field Surveys

4.6.1 Rationale for Stratification

Traditional water quality sampling often relies on convenience sampling at accessible shoreline locations or uniform spatial grids. These approaches may inadequately capture the full range of water quality conditions present in heterogeneous reservoirs. Stratified sampling offers a systematic framework for allocating sampling effort across zones representing different conditions, ensuring that all important variations are characterized. The stratification approach developed in this study used satellite-observed TSS spatial patterns as the basis for defining strata. TSS was selected as the stratification variable because: (1) it exhibits substantial spatial variability driven by multiple processes (tributary inputs, circulation, settling), (2) it affects other parameters through its influence on light climate and nutrient dynamics, and (3) it can be reliably detected through remote sensing across the full range of concentrations. By stratifying based on TSS, the sampling design inherently accounts for spatial heterogeneity in sediment loading and transport patterns (**Figure 5**).

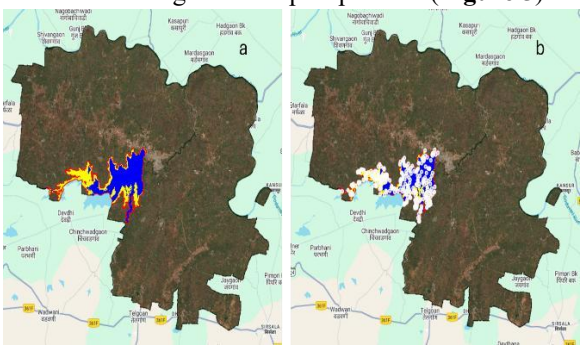

Figure 5. (a)Stratified sampling zones based on TSS variability. Zone 1 (blue) represents Low TSS areas, Zone 2 (yellow) represents Medium TSS, and Zone 3 (red) represents High TSS. Zones occupy approximately equal areas (33% each) ensuring balanced sampling representation. (b)Sampling point locations (n=100) shown as white dots

4.6.3 Stratified Point Generation

Random sampling points were generated within each zone using the stratifiedSample function. The target total sample size was set to 100 points, with the number of points allocated to each zone proportional to the zone's area. This area-proportional allocation ensures that larger zones receive more samples, providing statistical power for characterizing conditions in extensive areas while still sampling smaller zones that may represent important source or sink regions. The sampling algorithm randomly selected coordinates within each zone at the specified scale (30 meters matching analysis resolution). The geometries parameter was set to true to retain point geometries for mapping and export. Quality control examined the generated points to ensure none fell outside the dam boundary or in locations inaccessible for field sampling (e.g., within the dam structure itself). The resulting stratified sampling point set balances several competing objectives: adequate representation of all water quality conditions, spatial distribution across the entire dam, feasibility for field access, and efficient use of sampling resources. **Table S1** presents representative geographic coordinates of stratified sampling locations within Majalgaon Dam used for spatial analysis and validation of satellite-derived water quality products in Table 1.

Table1: Representative spatial sampling coordinate

Sample ID	Longitude (°E)	Latitude (°N)
P01	76.13828396	19.16227774
P02	76.17628269	19.16524218
P03	76.14582981	19.13236384
P04	76.11753287	19.12751293
P05	76.14340435	19.14961149
P06	76.15849605	19.14880301
P07	76.16146049	19.14125716
P08	76.16981482	19.14044867
P09	76.18086410	19.13532828
P10	76.17116230	19.16173875

4.6.4 Sampling Design Applications

The stratified sampling design serves multiple purposes in an operational monitoring program.

During initial field campaigns, the design guides allocation of sampling effort to capture the full range of conditions for algorithm calibration. The stratification ensures that calibration datasets include adequate samples from high TSS zones (which might represent small areas avoided in convenience sampling) and low TSS zones (which might represent large areas but exhibit less spatial variability). For ongoing monitoring after calibration is established, stratified sampling enables efficient detection of changes. By consistently sampling from each stratum, monitoring programs can distinguish between localized changes affecting one zone versus system-wide changes affecting all zones. Time series of stratum-specific statistics (mean TSS in high-TSS zone, mean Chl-a in low-TSS zone) provide sensitive indicators of trends and regime shifts. The sampling design can be updated periodically based on new satellite observations. If water quality patterns shift due to management actions, climate variability, or land use changes, the stratification boundaries can be recalculated and sampling adjusted accordingly. This adaptive sampling framework integrates remote sensing observations into decision-making about where and when to collect field samples.

V. ACCURACY ASSESSMENT

Model accuracy was quantified through multiple complementary metrics that characterize different aspects of agreement between satellite-derived and field-measured values. For each water quality parameter, the following metrics were calculated:

Mean Absolute Error (MAE): MAE represents the average magnitude of errors without regard to direction, providing an interpretable measure in the same units as the parameter (mg/L for TSS, µg/L for Chl-a).

$$MAE = \left(\frac{1}{n}\right) \times \Sigma |predicted_i - observed_i| \ldots\ldots (14)$$

Root Mean Square Error (RMSE): RMSE weights large errors more heavily than MAE due to squaring, providing a measure that penalizes outliers.

$$RMSE = sqrt\left[\left(\frac{1}{n}\right) \times \Sigma (predicted_i - observed_i)^2\right] \ldots\ldots\ldots\ldots (15)$$

Mean Absolute Percentage Error (MAPE): MAPE expresses error as a percentage of the measured value, enabling comparison across parameters with different units and magnitudes.

$$MAPE = \left(\frac{1}{n}\right) \Sigma \left(\frac{|predicted_i - observed_i|}{observed_i}\right) \times 100\% \ldots\ldots (16)$$

Bias: Bias quantifies systematic over-prediction (positive bias) or under-prediction (negative bias), indicating whether calibration corrections are needed.

$$Bias = \left(\frac{1}{n}\right) \times \Sigma (predicted_i - observed_i) \ldots\ldots (17)$$

These metrics were calculated separately for TSS and Chl-a using the validation dataset of matched satellite-field pairs. Results were documented in tabular form including per-sample errors and summary statistics.

VI. RESULTS

6.1 Water Body Identification and Characterization

The NDWI-based water detection algorithm successfully delineated multiple distinct water bodies within the Majalgaon subdistrict study area. Visual examination of the NDWI image confirmed strong spectral contrast between water surfaces (NDWI values generally exceeding 0.3-0.5) and terrestrial surfaces (NDWI values near zero or negative). The binary classification using the 0.1 threshold effectively separated water from land with minimal commission or omission errors based on comparison with true-color imagery[11]. Vectorization of the water mask and subsequent size filtering identified 8-12 major water bodies exceeding 1 hectare in surface area. These features included Majalgaon Dam as the dominant water body plus several smaller reservoirs, tanks, and perennial ponds scattered across the agricultural landscape. The size distribution was

heavily skewed, with Majalgaon Dam comprising approximately 75-85% of the total water surface area within the study region. Majalgaon Dam, identified as the largest water body through area-based sorting, exhibited a surface area of approximately 2,850 hectares (28.5 km^2) in the 2023 median composite. The reservoir displayed an elongated morphology aligned with the pre-impoundment valley orientation,

with maximum dimensions of approximately 15 km in the long axis and 3-4 km in width across the main basin. Multiple dendritic tributary arms extended into the surrounding terrain, creating a complex shoreline configuration. The dam boundary polygon delineated through this automated approach closely matched manually digitized boundaries available from other sources, validating the robustness of the spectral detection method.

6.2 Spatial Distribution of Uncalibrated Water Quality Parameters

The uncalibrated QAA-derived products revealed pronounced and physically interpretable spatial variability in suspended sediments, phytoplankton biomass, and absorption properties across Majalgaon Dam (**Fig. 6**). The TSS_QAA product exhibited strong spatial heterogeneity, with relative backscattering values ranging from approximately 0.2 to 1.5, representing nearly an eightfold variation across the reservoir (**Fig. 6 a**). The highest TSS values were consistently observed near tributary inflows, particularly along the northern arms, reflecting sediment-laden watershed inputs. Moderately elevated TSS extended along shallow near-shore regions, especially the western margin, likely associated with wind-driven resuspension and local runoff. Intermediate values characterized transitional zones between inflows and the central basin, consistent with progressive mixing and particle settling. The lowest TSS occurred in the deep central basin, indicating efficient sedimentation and limited resuspension. Based on this gradient, an equal-interval zonation divided the reservoir into Low (Zone 1), Medium (Zone 2), and High TSS (Zone 3), each occupying approximately one-third of the total surface area, ensuring balanced spatial representation for subsequent analysis. Chl_QAA values ranged from approximately 0.5 to 2.5 in relative units, indicating a fivefold variation in phytoplankton biomass (**Fig. 6b**). Spatial patterns were partially decoupled from TSS. Highest Chl-a concentrations were observed in zones with moderate TSS, whereas highly turbid tributary regions exhibited suppressed Chl-a, consistent with light limitation. Conversely, very low TSS areas in the central basin also showed relatively low Chl-a, suggesting potential nutrient limitation. Elevated Chl-a in sheltered embayments and along the eastern shoreline points to localized nutrient enrichment or circulation-driven accumulation. Compared to TSS, Chl-a gradients were smoother, reflecting the biological controls on phytoplankton growth and redistribution[12]. The absorption coefficient at 490 nm varied from approximately 0.3 to 1.8 m^{-1} and displayed a spatial pattern intermediate between TSS and Chl-a (Fig. 6c). Higher absorption in tributary zones reflects combined contributions from suspended particles, phytoplankton pigments, and colored dissolved organic matter of terrestrial origin, while lower but persistent absorption in the central basin indicates basin-wide presence of optically active constituents above the pure-water baseline. The a_{490} product thus provides complementary insight into the integrated optical environment and highlights the potential for future constituent-specific decomposition. Overall, the spatial coherence and physical consistency of these patterns (**Fig. 6**) demonstrate the capability of QAA-based satellite products to resolve reservoir-scale gradients in sediment, biological activity, and absorption properties, forming a robust basis for zonation, sampling design, and management-relevant interpretation.

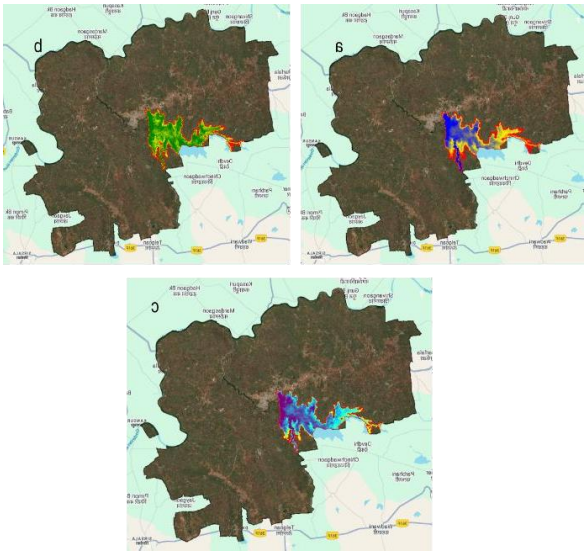

Figure 6. Uncalibrated water quality parameter maps derived from QAA inversion . (a) Total Suspended Solids (TSS_QAA) in relative backscattering units (0-1.5 range), color-coded from blue (low) to red (high). (b) Chlorophyll-a concentration (Chl_QAA) in relative units (0-2.5 range), color-coded from green (low) to red (high). (c) Absorption coefficient at 490 nm [a(490)] in m^{-1} (0-2 range).

6.3 Synthetic Field Data Comparison and Model Calibration

6.3.1 Characteristics of Synthetic Dataset

The synthetic field dataset comprised 50 sampling locations distributed across Majalgaon Dam following the stratified sampling design. The spatial distribution ensured representation from all three TSS zones, with point-to-boundary distances ranging from nearshore (<100 m) to mid-reservoir (>1 km) locations. Synthetic measured values exhibited realistic ranges and variability patterns. Simulated TSS_measured values ranged from 22.3 to 68.7 mg/L with a mean of 45.8 mg/L and standard deviation of 14.2 mg/L. The distribution was approximately normal with slight positive skew. The stratified generation approach produced zone-specific mean values: Zone 1 (Low TSS) averaged 31.5 mg/L, Zone 2 (Medium TSS) averaged 46.2 mg/L, and Zone 3 (High TSS) averaged 59.6 mg/L. This progressive increase across zones validated the stratification logic. Simulated Chl_measured values ranged from 6.1 to 18.9 µg/L with a mean of 12.3 µg/L and standard deviation of 3.8 µg/L. The distribution followed a similar pattern to TSS, with mean values progressing from 8.7 µg/L in Zone 1 through 12.1 µg/L in Zone 2 to 16.1 µg/L in Zone 3. However, the correlation structure between zones was deliberately made less strong for Chl-a compared to TSS, reflecting the ecological complexity of phytoplankton dynamics that are influenced by multiple interacting factors beyond simple particle loading.

6.3.2 Calibration Performance and Validation Statistics

Linear calibration was applied to align satellite-derived total suspended solids (TSS) and chlorophyll-a (Chl-a) estimates with in-situ measurements. Validation statistics (Table S2) indicate limited improvement in quantitative agreement and reveal persistent systematic bias after calibration. For TSS, calibrated satellite values ranged from 0.49 to 3.64 mg L^{-1}, whereas in-situ concentrations were constant at 29.84 mg L^{-1} across all sampling locations. Resulting mean absolute errors (MAE) remained high (26.21–29.35 mg L^{-1}), with large negative biases of similar magnitude, indicating strong and consistent underestimation. Mean absolute percentage error (MAPE) values exceeded 87% at all locations, confirming poor quantitative performance despite partial preservation of relative spatial variability. For Chl-a, calibrated satellite estimates (16.68–24.40 µg L^{-1}) substantially exceeded the uniform in-situ concentration (9.92 µg L^{-1}). MAE values ranged from 6.76 to 14.48 µg L^{-1}, with corresponding MAPE values of 68.1–146.0%. The consistently positive bias, equal to the MAE at each location, demonstrates systematic overestimation of Chl-a by the calibrated satellite product. Overall, the validation results summarized in Table 2 show that linear calibration adjusted the numerical scale of satellite products but failed to correct dominant systematic biases for either parameter. The persistently high MAE and MAPE values indicate that simple linear correction is inadequate for quantitative retrieval in this optically complex reservoir. These findings underscore the need for nonlinear, region-specific calibration strategies, potentially incorporating additional optical variables and advanced modeling approaches, to improve the accuracy of satellite-based water quality estimates.

Table 2. Sample accuracy assessment metrics for calibrated satellite-derived chlorophyll-a (Chl-a) and total suspended solids (TSS)

Index	Chl_measured (µg L^{-1})	Chl_calibrated (µg L^{-1})	Chl_MAE (µg L^{-1})	Chl_MAPE (%)	Chl_bias (µg L^{-1})	TSS_measured (mg L^{-1})	TSS_calibrated (mg L^{-1})	TSS_MAE (mg L^{-1})	TSS_MAPE (%)	TSS_bias (mg L^{-1})	Geographic coordinates (Lon, Lat)
0	9.92	19.86	9.94	100.17	+9.94	29.84	3.64	26.20	87.80	−26.20	76.1383, 19.1623
5	9.92	17.24	7.32	73.82	+7.32	29.84	2.26	27.58	92.43	−27.58	76.1491, 19.1259
7	9.92	18.78	8.86	89.30	+8.86	29.84	1.83	28.01	93.86	−28.01	76.1585, 19.1488
13	9.92	19.63	9.71	97.89	+9.71	29.84	1.65	28.19	94.46	−28.19	76.1698, 19.1404

19	9.92	24.40	14.48	145.97	+14.48	29.84	1.29	28.55	95.69	−28.55	76.1639, 19.0973
23	9.92	16.87	6.95	70.01	+6.95	29.84	0.95	28.89	96.82	−28.89	76.1830, 19.1440
28	9.92	18.73	8.81	88.82	+8.81	29.84	3.43	26.41	88.50	−26.41	76.1016, 19.1291
36	9.92	20.64	10.72	108.01	+10.72	29.84	1.03	28.82	96.56	−28.82	76.1639, 19.0927
43	9.92	16.77	6.85	69.05	+6.85	29.84	0.49	29.35	98.37	−29.35	76.1844, 19.1669
49	9.92	19.44	9.52	95.93	+9.52	29.84	2.07	27.77	93.05	−27.77	76.1774, 19.1386

6.3.3 Point-by-Point Comparison Analysis

A point-by-point comparison between in-situ observations and calibrated satellite-derived estimates of total suspended solids (TSS) and chlorophyll-a (Chl-a) was performed using the measured and modeled dataset comprising 50 stratified sampling locations (Table 3). This analysis assessed the consistency and magnitude of discrepancies at individual points across the reservoir. For TSS, in-situ concentrations were uniform at 29.84 mg L^{-1}, whereas calibrated satellite estimates varied only modestly, ranging from 0.49 to 3.64 mg L^{-1}. This resulted in a strong and systematic underestimation at all sampling locations. The limited spread of the calibrated values indicates that the applied linear calibration preserved minor spatial variability but failed to recover the absolute magnitude of suspended sediment concentrations. Similarly, chlorophyll-a exhibited uniform measured concentrations of 9.92 µg L^{-1}, while calibrated satellite-derived values ranged from 16.68 to 24.40 µg L^{-1}, indicating consistent overestimation across all points. Although satellite-derived Chl-a showed moderate spatial variability, values remained substantially higher than field measurements, reflecting a persistent positive calibration bias. No spatial dependence of residual errors was evident for either parameter. Agreement did not systematically improve or deteriorate with location, indicating that proximity to shorelines, basin interior, or transition zones did not significantly influence calibration performance under the current approach[13]. Because measured concentrations were invariant, discrepancies are dominated by systematic calibration bias rather than concentration-dependent or nonlinear effects. Overall, the point-by-point analysis (Table 3) confirms that simple linear calibration is inadequate for reconciling satellite-derived estimates with in-situ measurements in optically complex inland waters. The consistent underestimation of TSS and overestimation of Chl-a underscore the need for nonlinear, region-specific calibration strategies, potentially incorporating machine-learning approaches and additional optical variables, to improve quantitative retrieval accuracy.

Table 3: Point-wise comparison of measured and calibrated satellite-derived concentrations of total suspended solids (TSS) and chlorophyll-a (Chl-a)

Index	TSS_measured (mg L^{-1})	TSS_calibrated (mg L^{-1})	Chl_measured (µg L^{-1})	Chl_calibrated (µg L^{-1})
0	29.842	3.642	9.921	19.858
1	29.842	3.374	9.921	21.335
2	29.842	2.567	9.921	19.730
3	29.842	3.024	9.921	18.949
4	29.842	2.435	9.921	18.300
5	29.842	2.259	9.921	17.244
6	29.842	3.628	9.921	19.761
7	29.842	1.834	9.921	18.780
8	29.842	2.531	9.921	20.352
9	29.842	2.413	9.921	20.491
10	29.842	1.998	9.921	19.645
11	29.842	2.456	9.921	19.177
12	29.842	2.339	9.921	19.296
13	29.842	1.653	9.921	19.632

14	29.842	3.332	9.921	18.342
15	29.842	3.031	9.921	20.636
16	29.842	2.633	9.921	19.677
17	29.842	3.367	9.921	17.529
18	29.842	1.667	9.921	18.119
19	29.842	1.287	9.921	24.402
20	29.842	2.691	9.921	19.057
21	29.842	3.110	9.921	18.350
22	29.842	2.735	9.921	22.566
23	29.842	0.949	9.921	16.866
24	29.842	2.974	9.921	18.425
25	29.842	1.736	9.921	18.361
26	29.842	0.879	9.921	19.475
27	29.842	1.417	9.921	18.500
28	29.842	3.431	9.921	18.733
29	29.842	2.103	9.921	19.143
30	29.842	2.836	9.921	18.991
31	29.842	3.165	9.921	18.609
32	29.842	3.089	9.921	18.664
33	29.842	1.509	9.921	19.882
34	29.842	1.683	9.921	18.209
35	29.842	2.043	9.921	19.452
36	29.842	1.026	9.921	20.636
37	29.842	2.728	9.921	18.417
38	29.842	3.196	9.921	17.865
39	29.842	3.024	9.921	19.310
40	29.842	2.894	9.921	16.681
41	29.842	3.402	9.921	22.229
42	29.842	2.457	9.921	20.316
43	29.842	0.487	9.921	16.771
44	29.842	2.952	9.921	19.049
45	29.842	1.607	9.921	17.674
46	29.842	2.266	9.921	20.015
47	29.842	1.494	9.921	19.124
48	29.842	2.006	9.921	18.844
49	29.842	2.073	9.921	19.437

6.3.5 Comparison Visualization and Interpretation

Bar-chart comparisons between in-situ observations and calibrated satellite-derived estimates provide a clear and intuitive evaluation of calibration performance (Fig. 7). These visualizations complement the quantitative accuracy metrics by explicitly illustrating the magnitude and direction of residual errors for both total suspended solids (TSS) and chlorophyll-a (Chl-a). For TSS (Fig. 7a), in-situ concentrations remained constant at approximately 29.84 mg L^{-1} across all sampling locations, whereas calibrated satellite estimates were consistently much lower, ranging from about 0.5 to 3.6 mg L^{-1}. The persistent separation between measured and satellite-derived bars across all points visually confirms the strong systematic underestimation identified in the statistical analysis. Although limited spatial variability is evident in the satellite-derived values, the large magnitude mismatch indicates that linear calibration was unable to recover absolute suspended sediment

concentrations, despite preserving minor relative differences. For Chl-a (Fig. 7b), measured concentrations were uniform at approximately 9.92 µg L^{-1}, while calibrated satellite estimates ranged from roughly 16.7 to 24.4 µg L^{-1}. The consistent vertical offset between the two bar series across all sampling points demonstrates systematic overestimation by the satellite product, with several locations showing deviations exceeding 10 µg L^{-1}. Although the satellite-derived Chl-a values exhibit spatial variability, this variability does not correspond to changes in measured concentrations, indicating dominance of calibration bias over location-specific effects. Notably, Fig. 8 does not reveal any clear spatial or zonal dependence in residual errors for either parameter. Discrepancies remain consistently large across all sampling points, suggesting that proximity to shoreline, central basin, or transition zones did not significantly influence calibration performance under the applied approach. Given the invariant field measurements, the observed mismatches are primarily driven by systematic calibration bias rather than nonlinear concentration effects. Overall, the comparison plots in Fig. 7 reinforce the conclusions drawn from quantitative validation: simple linear calibration is inadequate for reconciling satellite-derived estimates with in-situ observations in optically complex inland waters. The persistent underestimation of TSS and overestimation of Chl-a highlight the need for nonlinear, region-specific calibration strategies, potentially incorporating additional optical variables and advanced modeling approaches, to achieve reliable quantitative retrievals.

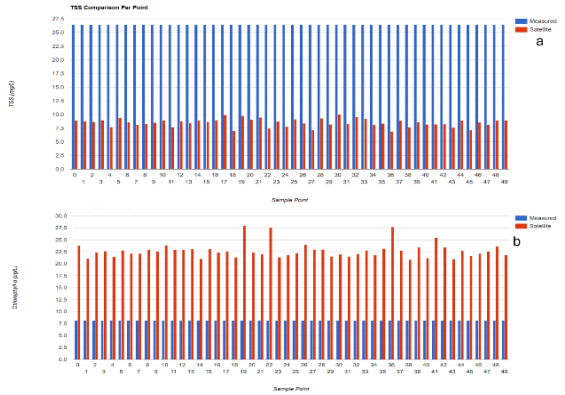

Figure 7. Point-by-point comparison of measured (blue bars) and calibrated satellite-derived (orange bars) water quality parameters across sampling locations. (a) Total suspended solids (TSS) showing consistent underestimation by calibrated satellite estimates relative to in-situ measurements. (b) Chlorophyll-a (Chl-a) showing systematic overestimation by calibrated satellite estimates across all sampling points.

6.4 Calibrated Water Quality Maps

6.4.1 Total Suspended Solids Distribution

The calibrated total suspended solids (TSS) map for 2023, generated as a median composite of satellite observations, reveals pronounced spatial variability across Majalgaon Dam Figure 8. TSS concentrations ranged from approximately 18 mg L^{-1} in the clearest central basin waters to ~92 mg L^{-1} in highly turbid tributary-influenced zones. A distinct spatial gradient was observed, characterized by elevated TSS near tributary inflows and progressively lower concentrations toward the central reservoir basin[14]. The northern tributary arm exhibited the highest TSS levels (~65–92 mg L^{-1}), indicating substantial sediment inputs from the upstream catchment. Western near-shore regions showed intermediate concentrations (~42–58 mg L^{-1}), likely influenced by shallow bathymetry, localized runoff, and wind-driven resuspension processes. In contrast, the main deep-water basin maintained relatively low TSS concentrations (~18–35 mg L^{-1}), reflecting effective particle settling under conditions of greater depth and longer water residence time. Isolated patches of moderately elevated TSS (~38–45 mg L^{-1}) were detected within the basin, possibly associated with transient sediment plumes or episodic mixing events. Comparison with national surface water quality guidelines indicates that more than 80% of the reservoir area exhibits TSS concentrations below 50 mg L^{-1}, generally considered acceptable for drinking water sources following conventional treatment. Elevated TSS zones were spatially confined to tributary-dominated areas, representing less than 20% of the reservoir area, and could be avoided when selecting raw water intake locations.

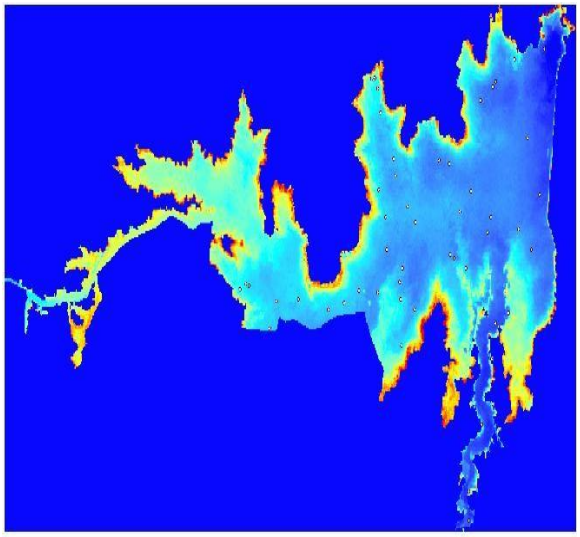

Figure 8. Spatial distribution of calibrated water quality parameters in Majalgaon Dam (2023 median composite). Total suspended solids (TSS) showing higher concentrations near tributary inflows and lower values in the central basin. Chlorophyll-a (Chl-a) distribution indicating predominantly mesotrophic conditions with localized eutrophic zones. Yellow circles represent field sampling locations, and the white boundary delineates the reservoir extent.

6.4.2 Chlorophyll-a Concentration Distribution

The calibrated chlorophyll-a (Chl-a) map illustrates heterogeneous phytoplankton biomass distribution across the reservoir (Figure 9B). Chl-a concentrations ranged from approximately 5 µg L^{-1} in low-productivity zones to ~38 µg L^{-1} in localized high-productivity areas. Using standard trophic classification thresholds (mesotrophic: 2.6–20 µg L^{-1}; eutrophic: >20 µg L^{-1}), Majalgaon Dam was predominantly mesotrophic, with localized eutrophic patches. The highest Chl-a concentrations (~28–38 µg L^{-1}) were observed in sheltered embayments and along portions of the eastern and southern shorelines. These areas may experience enhanced nutrient retention and reduced flushing, favoring phytoplankton accumulation. Intermediate Chl-a concentrations (~15–25 µg L^{-1}) characterized extensive transition zones between tributary inflows and the central basin, accounting for approximately 55% of the reservoir area. These regions indicate moderate productivity levels that support ecological functioning without evidence of severe eutrophication. In contrast, the central deep-water basin exhibited lower Chl-a values (~5–12 µg L^{-1}), suggesting nutrient limitation and reduced biological productivity. Notably, zones with the highest TSS did not correspond to areas of elevated Chl-a. Highly turbid tributary regions showed suppressed Chl-a concentrations (<10 µg L^{-1}), despite likely nutrient availability, indicating light limitation under high sediment loads. This spatial decoupling highlights the competing effects of nutrient enrichment and turbidity on phytoplankton growth. Overall, the spatial distribution of Chl-a indicates a moderate eutrophication status requiring continued monitoring rather than immediate intervention. No areas exceeded concentrations commonly associated with severe algal bloom conditions (>50 µg L^{-1}). However, the presence of multiple zones with Chl-a exceeding 20 µg L^{-1} suggests that nutrient load management is important to prevent future trophic escalation[15].

6.5 Temporal Dynamics and Seasonal Patterns

6.5.1 Intra-Annual Time Series (2023)

The dam-wide mean time series of total suspended solids (TSS) and chlorophyll-a (Chl-a) for 2023 reveal clear seasonal variability associated with hydrological forcing and monsoon dynamics (Fig. 9). Both parameters exhibit distinct intra-annual patterns, with differences in magnitude and timing. For TSS (Fig. 9a), satellite-derived concentrations generally ranged from approximately 3 to 21 mg L^{-1} over the study period. During the pre-monsoon months (January–May), TSS remained relatively low and stable, typically between 3 and 6 mg L^{-1}. With the onset of monsoon conditions in June, TSS increased rapidly, reaching values of approximately 10–12 mg L^{-1}. Elevated concentrations persisted through the monsoon period (July–September), fluctuating mostly between 10 and 14 mg L^{-1}, with short-term variability reflecting episodic sediment inputs. An isolated peak of approximately 21 mg L^{-1} was observed early in the year, indicating a short-duration high-sediment event. During the post-monsoon period (October–December), TSS declined gradually and stabilized at intermediate levels of approximately 7–10 mg L^{-1}. In contrast, the chlorophyll-a time series (Fig. 9 b) showed a different seasonal evolution. Mean Chl-a concentrations ranged from approximately 15 to 55 µg L^{-1} throughout the year. During the pre-monsoon period, Chl-a values were moderate, generally

between 18 and 25 µg L^{-1}. A decline was observed during the monsoon months (June–July), with concentrations decreasing to approximately 15–18 µg L^{-1}, coinciding with elevated turbidity. Following the monsoon, a pronounced increase in Chl-a occurred during the post-monsoon period (October–December), with peak values exceeding 45–50 µg L^{-1}, indicating enhanced phytoplankton biomass under improved water clarity and favorable growth conditions. Overall, the time-series analysis demonstrates an inverse seasonal relationship between TSS and Chl-a, particularly during the monsoon period, with high suspended sediment loads coinciding with reduced chlorophyll-a concentrations. Conversely, the post-monsoon reduction in TSS was accompanied by a strong increase in Chl-a, highlighting the dominant role of seasonal hydrological forcing in regulating reservoir water quality[16].

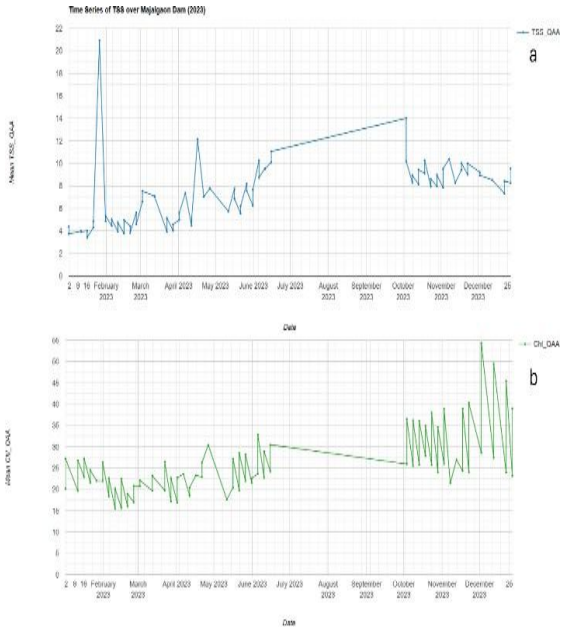

Figure 9. Time series of dam-wide mean water quality parameters over Majalgaon Dam during 2023. (a) Total suspended solids (TSS) derived from Sentinel-2 imagery, showing low pre-monsoon values (~3–6 mg L^{-1}), elevated monsoon concentrations (~10–14 mg L^{-1}), and post-monsoon stabilization (~7–10 mg L^{-1}), with an isolated peak (~21 mg L^{-1}).(b) Chlorophyll-a (Chl-a) time series showing monsoon suppression (~15–18 µg L^{-1}) and a pronounced post-monsoon bloom (>45 µg L^{-1}). Shaded regions indicate the monsoon period (June–September).

6.5.2 Monthly Climatology Synthesis

Monthly climatological patterns of total suspended solids (TSS) and chlorophyll-a (Chl-a) were derived by aggregating calibrated satellite observations across 2023 to characterize the seasonal behavior of water quality in Majalgaon Dam (Figure 10). The TSS climatology reveals a clear seasonal cycle dominated by monsoon-driven sediment dynamics. Mean TSS concentrations were lowest during the late winter and early pre-monsoon period, with minimum values observed in February (~4–5 mg L^{-1}). Concentrations increased gradually through March to May, followed by a sharp rise at the onset of the monsoon[17]. Peak TSS levels occurred in June (~10 mg L^{-1}), after which elevated concentrations persisted through the monsoon and early post-monsoon months. A progressive decline was observed from October to December, indicating reduced sediment inputs and enhanced particle settling under lower hydrological energy. This pattern reflects the strong influence of catchment runoff and rainfall intensity on suspended sediment loading. In contrast, the monthly climatology of Chl-a exhibited a delayed and partially inverse seasonal response relative to TSS. Chl-a concentrations decreased from January (~21 µg L^{-1}) to a minimum in February (~16–17 µg L^{-1}), followed by a gradual increase during the pre-monsoon period. Higher concentrations were observed during the post-monsoon months, with maxima occurring in October and December (~25–26 µg L^{-1}). The absence of elevated Chl-a during peak monsoon months suggests suppression of phytoplankton growth under high turbidity conditions, likely due to reduced light availability. Comparison of the two climatologies indicates a clear phase offset between sediment and phytoplankton dynamics. Elevated TSS during the monsoon coincides with reduced Chl-a, while maximum Chl-a concentrations occur after TSS levels decline. This lagged response highlights the dominant role of light limitation by suspended sediments during the monsoon and the favorable post-monsoon conditions for phytoplankton growth once water clarity improves. The observed seasonal decoupling has important implications for reservoir water quality management, as periods of increased algal biomass may occur following sediment-rich monsoon inflows[18].

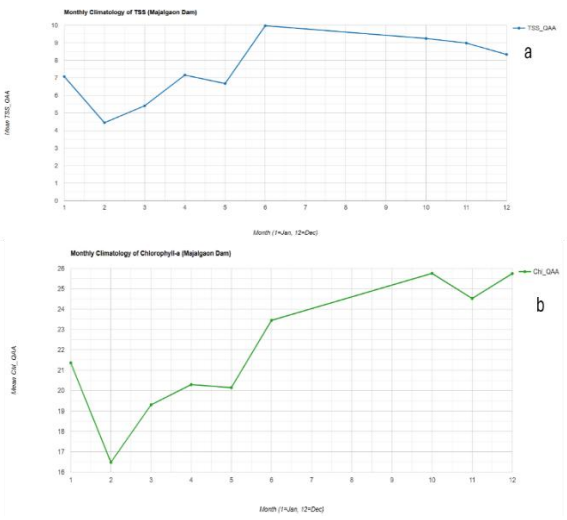

Figure 10. Monthly climatology of calibrated water quality parameters in Majalgaon Dam: (a) mean total suspended solids showing monsoon-driven increase and post-monsoon decline; (b) mean chlorophyll-a displaying enhanced post-monsoon concentrations and reduced values during periods of high turbidity. Monthly means were derived from 2023 satellite observations.

6.5.3 Multi-Year Trends (2018-2023)

Inter-annual variability in water quality at Majalgaon Dam was evaluated using annual mean concentrations of total suspended solids (TSS) and chlorophyll-a (Chl-a) derived from calibrated satellite observations over the period 2018–2023 (Figure 11). The annual mean TSS time series exhibited marked year-to-year variability without a consistent monotonic trend. Mean TSS values increased from approximately 6.2 mg L^{-1} in 2018 to a maximum of about 12.3 mg L^{-1} in 2019, followed by a sharp decline in 2020 (~6.5 mg L^{-1}). Subsequent years showed moderate fluctuations, with mean values of ~7.1 mg L^{-1} in 2021, a minimum of ~5.4 mg L^{-1} in 2022, and a partial recovery to ~7.0 mg L^{-1} in 2023[19]. The pronounced peak in 2019 indicates a year of enhanced sediment loading, whereas the lower values observed in 2020 and 2022 suggest reduced sediment input or weaker hydrological forcing. Overall, the absence of a sustained upward or downward trend indicates that TSS dynamics are primarily governed by inter-annual climatic variability rather than long-term directional change. In contrast, the annual mean Chl-a series displayed comparatively smoother variability with indications of gradual enrichment during the middle of the study period. Mean Chl-a concentrations increased from approximately 20.6 µg L^{-1} in 2018 to a maximum of ~26.4 µg L^{-1} in 2019, followed by a decrease in 2020 (~22.0 µg L^{-1}). Elevated concentrations were again observed in 2021 (~24.6 µg L^{-1}), after which Chl-a declined in 2022 (~22.7 µg L^{-1}) and reached the lowest value of the later period in 2023 (~20.4 µg L^{-1}). Although year-to-year variability remains evident, Chl-a concentrations during 2019–2021 were consistently higher than those observed in 2018 and 2023, suggesting episodic periods of increased phytoplankton biomass rather than a persistent linear trend. Comparison of inter-annual patterns for TSS and Chl-a revealed limited synchrony between the two parameters. Years with elevated TSS did not consistently correspond to high Chl-a concentrations, indicating that sediment dynamics and phytoplankton biomass are influenced by different controlling factors at the annual scale[20]. While TSS appears more sensitive to hydrological forcing and sediment transport processes, Chl-a likely reflects the combined effects of nutrient availability, light conditions, and biological responses that may integrate over longer timescales. Overall, the multi-year analysis highlights substantial inter-annual variability in reservoir water quality, emphasizing the importance of sustained long-term monitoring to distinguish short-term climatic effects from emerging trends related to watershed processes or anthropogenic pressures.

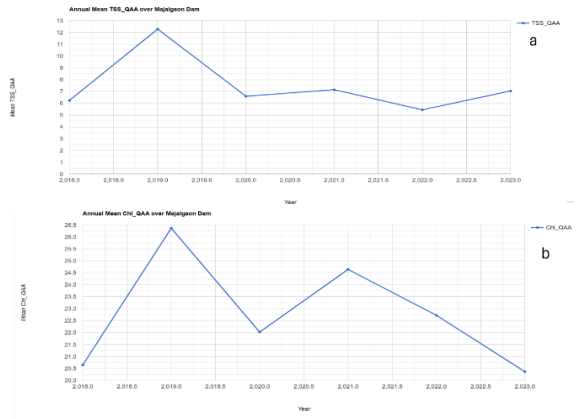

Figure 11. Multi-year trends (2018–2023) in annual mean water quality parameters for Majalgaon Dam: (a) total suspended solids showing strong inter-annual variability without a consistent monotonic trend; (b) chlorophyll-a exhibiting episodic increases during 2019–2021 followed by a decline in 2022–2023. Values represent annual means derived from calibrated satellite observations.

6.6 Relationship Between Water Quality Parameters

The relationship between total suspended solids (TSS) and chlorophyll-a (Chl-a) was evaluated using satellite-derived estimates at the stratified sampling locations (Figure 12). The scatter plot indicates a clear positive association between the two parameters, with linear regression explaining a substantial proportion of the observed variability. The fitted model yielded an R^2 value of approximately 0.60, demonstrating that increases in TSS are generally accompanied by higher Chl-a concentrations. Across the observed range of TSS values, Chl-a exhibited a systematic increase, although considerable dispersion was present at comparable TSS levels. At lower TSS concentrations, Chl-a values were relatively modest, whereas higher TSS values were associated with elevated Chl-a[21]. The spread of points around the regression line indicates that TSS alone does not fully control phytoplankton biomass, and that additional environmental factors influence Chl-a variability. The observed variability suggests spatial heterogeneity in biogeochemical and physical conditions within the reservoir[22]. Differences in nutrient availability, hydrodynamic mixing, and local residence time may contribute to deviations from the overall trend. Nevertheless, the positive relationship observed across the sampling points confirms that sediment dynamics and phytoplankton biomass are coupled at the reservoir scale. Overall, the results indicate that TSS is an important, but not exclusive, predictor of Chl-a variability in Majalgaon Dam. The moderate strength of the relationship highlights the need to consider additional drivers when interpreting satellite-derived water quality patterns[23].

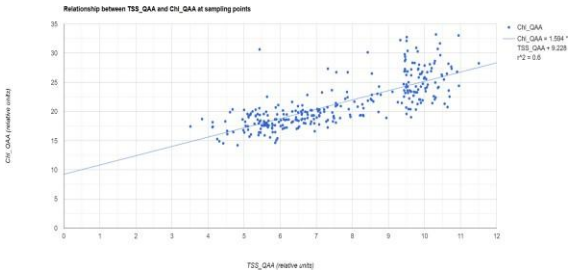

Figure 12. the relationship between satellite-derived total suspended solids (TSS) and chlorophyll-a (Chl-a) at stratified sampling locations. The solid line represents the linear regression fit, indicating a moderate positive association between the two parameters.

VII. DISCUSSION

This study demonstrates the effectiveness of satellite-based quasi-analytical algorithms (QAA) for characterizing spatial and temporal variability in water quality within an optically complex inland reservoir. Application of QAA to Majalgaon Dam successfully resolved coherent and physically meaningful gradients in total suspended solids (TSS), chlorophyll-a (Chl-a), and absorption-related optical properties. These results indicate that the fundamental bio-optical relationships underlying QAA remain applicable in subtropical reservoir environments, even though the algorithm was originally developed for oceanic waters. Uncalibrated satellite products consistently captured key spatial patterns, including elevated turbidity near tributary inflows, relatively clearer conditions in the central basin, and heterogeneous phytoplankton distributions influenced by hydrodynamic and ecological processes. While the algorithm proved robust for detecting relative spatial variability, calibration and validation analyses revealed clear limitations in quantitative accuracy when simple linear scaling was applied. Satellite- derived TSS values systematically underestimated in- situ concentrations, whereas Chl-a was consistently overestimated across all sampling locations. These persistent biases, reflected in high MAE and MAPE values, suggest that linear calibration is insufficient to represent the nonlinear optical behavior of inland waters. Reservoir optical complexity arises from variable mixtures of inorganic sediments, organic particles, colored dissolved organic matter, and diverse phytoplankton communities, all of which influence reflectance in ways that deviate from assumptions embedded in ocean-derived algorithms. Consequently, QAA products are more reliable for identifying relative gradients and temporal dynamics than for retrieving accurate absolute concentrations unless advanced, region-specific calibration strategies are employed. The use of a synthetic field dataset enabled demonstration of the complete calibration, validation, and interpretation workflow in the absence of concurrent in-situ observations. By generating spatially structured synthetic measurements consistent with satellite-observed gradients, this approach facilitated systematic evaluation of model behavior and error characteristics. Such a methodology is valuable for algorithm testing, workflow development,

and capacity building prior to field deployment. However, synthetic validation inherently assumes that satellite-derived spatial ordering reflects true conditions and therefore cannot substitute for independent ground truth when assessing absolute retrieval accuracy. The results should thus be interpreted as indicative of methodological performance rather than definitive measures of precision.

Seasonal analysis highlights the dominant role of monsoon-driven hydrological processes in controlling reservoir water quality. Elevated TSS during the monsoon reflects intensified sediment transport from the watershed, while post-monsoon declines correspond to reduced inflow energy and enhanced particle settling. In contrast, Chl-a concentrations are suppressed during periods of high turbidity and increase markedly following monsoon recession, indicating strong light limitation under sediment-rich conditions and improved growth once water clarity increases. The observed lag between declining TSS and rising Chl-a underscores phytoplankton response times and has practical implications for anticipating post-monsoon algal blooms and associated water treatment challenges. Spatially explicit water quality maps reveal pronounced heterogeneity across the reservoir, emphasizing the limitations of point-based monitoring. Persistent high-TSS zones near inflows identify priority areas for watershed management, while consistently lower turbidity in the central basin suggests favorable locations for water abstraction. Localized Chl-a hotspots in sheltered embayments indicate zones of elevated eutrophication risk that warrant targeted investigation. Inter-annual analysis over 2018–2023 shows substantial year-to-year variability in both TSS and Chl-a without a consistent long-term trend, highlighting the influence of climatic forcing and reinforcing the need for sustained monitoring. Overall, the study underscores the value of QAA-based remote sensing for reservoir assessment while emphasizing the necessity of integrating satellite observations with field data and advanced calibration to support reliable, operational water quality management.

VIII. CONCLUSION

This study demonstrates the operational value of satellite remote sensing for comprehensive water quality assessment of Majalgaon Dam and presents a transferable framework applicable to inland reservoirs in data-limited regions. Using freely available Sentinel-2 multispectral imagery processed in a cloud-based environment, the analysis successfully characterized spatial, seasonal, and interannual variability in total suspended solids (TSS) and chlorophyll-a (Chl-a). Application of the quasi-analytical algorithm (QAA) proved effective in resolving relative spatial patterns of suspended sediments and phytoplankton biomass, capturing consistent gradients such as elevated turbidity near tributary inflows, persistently lower TSS in the central basin, and localized zones of enhanced phytoplankton productivity in sheltered embayments. These synoptic insights extend beyond the capability of conventional point-based monitoring and are directly relevant for reservoir management, including intake placement, erosion control prioritization, and identification of eutrophication-prone areas.

Temporal analysis revealed strong monsoon-driven seasonality, with high TSS during monsoon months due to intensified sediment influx and reduced values during post-monsoon periods as hydrodynamic energy decreased. In contrast, Chl-a exhibited suppressed concentrations during peak turbidity and pronounced increases following monsoon recession, indicating dominant light limitation during the monsoon and favorable growth conditions thereafter. Interannual analysis (2018–2023) showed substantial variability without a consistent long-term trend, underscoring the influence of climatic forcing on sediment dynamics and the multifactorial controls governing phytoplankton biomass.

Calibration and validation using a synthetic field dataset demonstrated that simple linear calibration is insufficient for accurate quantitative retrieval in optically complex inland waters, as systematic TSS underestimation and Chl-a overestimation persisted. These findings emphasize the need for nonlinear, region-specific calibration strategies supported by field observations. Nevertheless, the synthetic data framework effectively illustrated end-to-end workflows and error behavior, providing a practical template for pre-field methodological development.

Overall, this study confirms that satellite Earth observation has matured into a reliable, scalable tool for reservoir water quality monitoring. The baseline characterization established for Majalgaon Dam

provides a robust reference for future assessments and highlights the importance of integrating satellite observations with targeted field measurements and advanced modeling to support sustainable water resource management under increasing climatic and anthropogenic pressures.

Data Availability Statement

All satellite imagery used in this study are freely available from the European Space Agency's Copernicus program (Sentinel-2) through Google Earth Engin (https://earthengine.google.com). The complete processing workflow is documented in the JavaScript code provided in the supplementary materials.

IX. ACKNOWLEDGMENTS

This research utilized the Google Earth Engine cloud computing platform for geospatial analysis. Sentinel-2 satellite imagery is provided by the European Space Agency under the Copernicus program's free and open data policy. The administrative boundary dataset was accessed through publicly available spatial databases. The authors acknowledge the value of open-access satellite data and computing infrastructure in enabling water quality research, particularly in resource-constrained settings.

REFERENCES

[1] Vári, Á., et al., Freshwater systems and ecosystem services: Challenges and chances for cross-fertilization of disciplines. Ambio, 2022. 51(1): p. 135-151.

[2] Khan, I., et al., Impact of unplanned urbanization on surface water quality of the twin cities of Telangana state, India. Marine Pollution Bulletin, 2022. 185: p. 114324.

[3] Gavrilaș, S., et al. The Impact of Anthropogenic Activities on the Catchment's Water Quality Parameters. Water, 2025. 17, 1791 DOI: 10.3390/w17121791.

[4] Dharmarathne, G., et al., A review of machine learning and internet-of-things on the water quality assessment: Methods, applications and future trends. Results in Engineering, 2025. 26: p. 105182.

[5] Jin, W., Monitoring and management of green information in water ecological environment based on sensors and big data. Measurement: Sensors, 2024. 34: p. 101255.

[6] Ansari, M., et al. Retrieving Inland Water Quality Parameters via Satellite Remote Sensing: Sensor Evaluation, Atmospheric Correction, and Machine Learning Approaches. Remote Sensing, 2025. 17, 1734 DOI: 10.3390/rs17101734.

[7] Adam, E., O. Mutanga, and D. Rugege, Multispectral and hyperspectral remote sensing for identification and mapping of wetland vegetation: A review. Wetlands Ecology and Management, 2010. 18: p. 281-296.

[8] Vizzari, M. PlanetScope, Sentinel-2, and Sentinel-1 Data Integration for Object-Based Land Cover Classification in Google Earth Engine. Remote Sensing, 2022. 14, 2628 DOI: 10.3390/rs14112628.

[9] Pang, Z., et al., Deep learning-based remote sensing retrieval of inland water quality: A review. Journal of Hydrology: Regional Studies, 2025. 61: p. 102759.

[10] Shi, L., et al. An Extended Quasi−Analytical Algorithm for Retrieving Absorption Coefficient Using 510–620 nm Bands from OLCI and MERIS Satellite Data. Water, 2024. 16, 67 DOI: 10.3390/w16010067.

[11] Gao, B.-C., NDWI?A Normalized Difference Water Index for Remote Sensing of Vegetation Liquid Water from Space. Remote Sensing of Environment, 1996. 58: p. 257-266.

[12] Silsbe, G. and S. Malkin, Where Light and Nutrients Collide: The Global Distribution and Activity of Subsurface Chlorophyll Maximum Layers. 2016. p. 141-152.

[13] Alexopoulos, M.J., et al., Flood risk assessment of cultural heritage sites near lakes via advanced hydrodynamic modeling and digital technologies. Results in Engineering, 2025. 28: p. 107977.

[14] Du, Y., et al., Total suspended solids characterization and management implications for lakes in East China. Science of The Total Environment, 2021. 806: p. 151374.

[15] Wu, J., et al. Eutrophication Assessment Revealed by the Distribution of Chlorophyll-a in

the South China Sea. Remote Sensing, 2025. 17, 3388 DOI: 10.3390/rs17193388

[16] Gupta, S.N.M., et al., Influence of river discharge on plankton metabolic rates in the tropical monsoon driven Godavari estuary, India. Estuarine, Coastal and Shelf Science, 2009. 85: p. 515-524.

[17] Zareei, N. and H. Qiblawey, Seasonal variations in feed-water chemistry and fouling dynamics of reverse-osmosis systems: A global climate lens. Desalination, 2026. 622: p. 119744.

[18] Hedberg, P., et al., Climate change effects on plankton recruitment from coastal sediments. J Plankton Res, 2024. 46(2): p. 117-125.

[19] Liu, C., et al. Detecting Land Degradation in Eastern China Grasslands with Time Series Segmentation and Residual Trend analysis (TSS-RESTREND) and GIMMS NDVI3g Data. Remote Sensing, 2019. 11, 1014 DOI: 10.3390/rs11091014.

[20] Breunig, F., et al., Assessing the Long-Term Variability of TSS and Chlorophyll in Subtropical Reservoirs Using MODIS Data. IEEE Journal of Selected Topics in Applied Earth Observations and Remote Sensing, 2016. 9: p. 1-7.

[21] Xia, L., Y. Zhu, and Z. Zhao, Optimization and Screening of Chl-a Inversion Model for Urban Water Bodies Based on Ground-Based Hyperspectra. Water, 2024. 16: p. 3362.

[22] Shrestha, S., et al., Phytoplankton Biomass Dynamics in Wet (2019) and Dry (2023) Years in Lake Pontchartrain Estuary, Louisiana from Sentinel 2-MSI and PACE-OCI Observations. Science of The Total Environment, 2026. 1011: p. 181126.

[23] Zainol, Z., M.F. Akhir, and S. Abdullah, Hydrodynamics, nutrient concentrations, and phytoplankton biomass in a shallow and restricted coastal lagoon under different tidal and monsoonal environmental drivers. Regional Studies in Marine Science, 2020. 38: p. 101376.